Estimation of snow water equivalent over first-year sea ice using AMSR-E and surface observations

A. Langlois [a,*], R. Scharien [b], T. Geldsetzer [b], J. Iacozza [a], D.G. Barber [a], J. Yackel [b]

[a] Centre for Earth Observation Science (CEOS), Department of Environment and Geography, University of Manitoba, Winnipeg, Canada R3T 2N2
[b] Department of Geography, University of Calgary, Calgary, Canada T2N 1N4

ABSTRACT

A SWE retrieval algorithm developed in-situ using passive microwave surface based radiometer data is applied to the Advanced Microwave Scanning Radiometer for Earth Observation System (AMSR-E). Snow water equivalent is predicted from two pixels located in Canadian Arctic Shelf Exchange Study (CASES) overwintering study area in Franklin Bay, N.W.T., Canada. Results show that the satellite SWE predictions are statistically valid with measured in-situ snow thickness data in both smooth and rough ice environments where predicted values range from 15 to 25 mm. Stronger correlation between measured and predicted data is found over smooth ice with R^2 value of 0.75 and 0.73 for both pixels respectively. Furthermore, a qualitative study of sea ice roughness using both passive and active microwave satellite data shows that the two pixels are rougher than the surrounding areas, but the SWE predictions do not seem to be affected significantly.

© 2008 Elsevier Inc. All rights reserved.

1. Introduction

Snow cover plays a primary role determining the thermodynamic state of the sea ice by controlling both radiative and mass transfers across the ocean-sea ice-atmosphere interface (e.g., Eiken, 2003). The surface energy balance (SEB) along with sea ice freeze-up and decay are strongly influenced by snow thickness and its thermophysical properties such as density, temperature, salinity and grain size (e.g., Langlois and Barber, 2007b). Given the recent dramatic ice depletion observed in the Arctic over the past three decades (Francis, Hunter, Key, Wang, 2005; Stroeve et al., 2005), global accurate snow measurements are required to assess the impact of the current and future changes in the Arctic environment.

Passive microwave satellite remote sensing is known as the best tool for regional snow thickness studies (Chang, Foster, Hall, 1987; Foster et al., 2005; Cordisco, Prigent, Aires, 2006) and recent results over sea ice are promising (Cavalieri and Comiso, 2004; Markus, Powell, Wang, 2006; Langlois and Barber, 2007a). Most of the satellite studies make use of a combination of 19 and 37 GHz channels to retrieve snow depth, whereas results from in-situ measurements using surface based radiometers (SBR) provide better predictions using single frequency/polarization algorithms (Barber, Iacozza, and Walker, 2003; Langlois, Barber, Hwang, 2007b).

One of the main challenges in global SWE retrieval studies over sea ice relates to spatial heterogeneity (e.g., Sturm et al., 2006). For instance, brightness temperatures from the Advanced Microwave Scanning Radiometer for Earth Observing System (AMSR-E) include emission contributions from different surface features (smooth ice, rough ice, open water) found in a pixel of 12.5×12.5 km (e.g., Mäkynen and Hallikainen, 2005) that can potentially alter SWE predictions thus, the effect of ice roughness on existing algorithms needs to be addressed.

With increasing ice roughness, the scattering increases and the polarization effect is expected to decrease (e.g., Mätzler, 1987; Eppler, 1992). Hence, the discrimination between smooth ice and ice ridges is possible due to the strong polarization effect of a layered snowpack (e.g., Garrity, 1992). Previous results from Kurvonen and Hallikainen (1997) showed good detection of deformed ice and old level ice using a combination of high (94 GHz) and low (24 or 34 GHz) frequencies airborne brightness temperature data. Furthermore, Mäkynen and Hallikainen (2005) investigated the effect of ice deformation on the passive microwaves polarization ratio (PR) and gradient ratio (GR) for different types of snow covers. Their results showed that the polarization ratio decreases with increasing ice roughness for both dry and moist snow but they had no success in discriminating all ice types. The combination of passive microwave brightness temperatures along with synthetic aperture radar (SAR) backscatter information
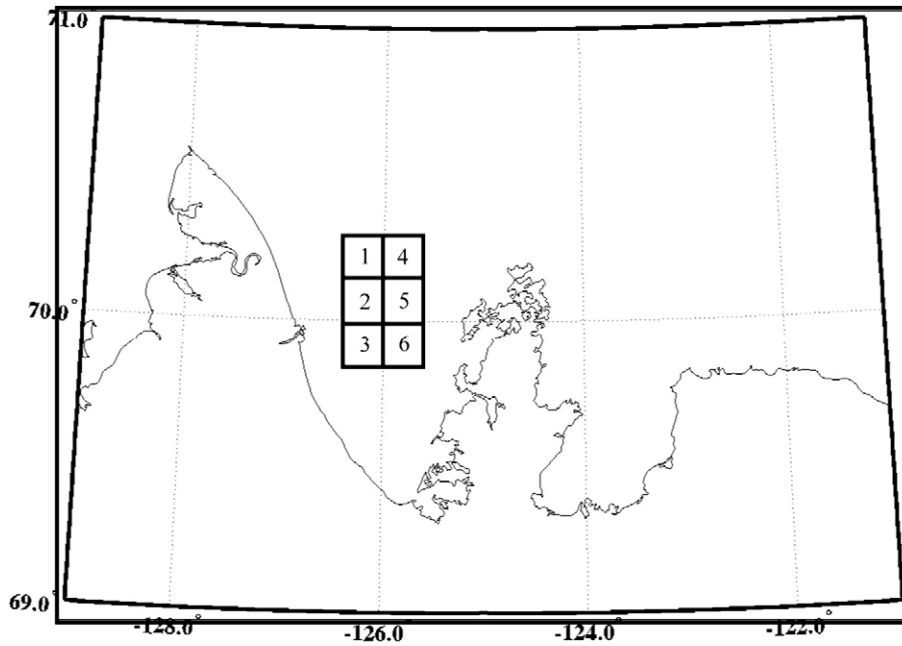
Fig. 1. AMSR-E pixel location within Franklin Bay, N.W.T.

could improve sea ice roughness information and very few studies have looked into this issue.

Therefore, the objectives of this paper are to a) apply the SWE algorithm developed from in-situ data by Langlois and Barber (2007a) to AMSR-E satellite data, b) to validate the predictions with in-situ measured snow thickness data, and c) to evaluate the effect of surface roughness on the SWE predictions using a combination of passive and active microwave data.

2. Data and methods

2.1. Study location

The study period extended between day 343 (December 7th, 2003) and 122 (April 30th, 2004) during the Canadian Arctic Shelf Exchange Study (CASES), in Franklin Bay, Northwest Territories, Canada. The Canadian Coast Guard icebreaker C.C.G.S. Amundsen was frozen into a pan of smooth ice where all the physical sampling occurred (Langlois, Mundy, Barber, 2007a). We used brightness temperatures from 6 adjacent pixels (12.5 km resolution) from AMSR-E within the bay (Fig. 1). The central coordinates of these pixels are displayed in Table 1.

2.2. Snow thickness

A series of thickness transects were conducted in different ice roughness conditions, and have been used for validation of the SWE predictions. Snow thickness lines were sampled at 0° (E–W direction), 45°, 90° (N–S direction) and 135° at a sampling interval of 1 m following a method developed by Iacozza and Barber (2001). The

sampled zone for SWE transects was 50×50 m, with sampling lines varying between 50 and 71 m from the directions mentioned above. The total number of samples varied between 483 and 500 for smooth transects as it varied between 477 and 505 for rough transects. We calculated SWE for the snow thickness measurements by incorporating density profiles measured at the ship's sampling site (Langlois et al., 2007a) over the same period and thickness range. Since the ship's was located in a smooth area, most of smooth SWE transects occurred near the ship between 0.19 km and 2.05 km distance (average of 1.32 km on Table 2). Rough ice SWE transects were located at a distance varying between 1.06 km and 2.63 km (average of 1.95 km on Table 3).

2.3. AMSR-E brightness temperatures

Brightness temperatures, T_b, were extracted from AMSR-E at both 18.7 and 36.5 GHz. The sensor was launched on the National Aeronautics and Space Administration (NASA) Aqua satellite (polar/sun-synchronous orbit) in May of 2002. The sensor collects data at six frequencies (6.9, 10.7, 18.7, 36.5, and 89 GHz in both horizontal and

Table 1
Coordinates of the AMSR-E pixels

Pixel 1	70.0403 N	−125.9421 W
Pixel 2	69.9296 N	−125.9934 W
Pixel 3	69.8190 N	−126.0442 W
Pixel 4	70.0223 N	−125.6185 W
Pixel 5	69.9118 N	−125.7241 W
Pixel 6	69.8013 N	−125.7241 W

Table 2
Basic SWE statistical data calculated from smooth ice snow thickness data

ID	Day	Latitude	Longitude	Transects SWE				AMSR-E SWE	
				Min	Max	Mean	SD	p-Min	p-Max
1	21	70.033	−126.342	11.3	18.7	12.9	11.0	16.1	16.3
2	24	70.043	−126.258	11.5	27.6	15.6	13.5	15.3	15.8
3	28	70.04	−126.26	11.7	25.9	14.5	13.0	18.0	18.5
4	32	70.041	−126.255	11.8	27.4	15.6	13.8	15.9	16.2
5	40	70.048	−126.255	11.7	34.1	16.5	13.6	17.4	17.9
6	48	70.051	−126.313	11.2	28.4	14.2	13.0	16.4	16.9
7	57	70.052	−126.3	12.6	26.6	15.4	12.8	17.0	17.9
8	65	70.052	−126.302	11.0	38.0	14.9	13.5	15.6	16.0
9	71	70.042	−126.302	11.7	34.1	15.7	14.0	15.2	15.5
10	76	70.051	−126.271	12.6	37.6	16	13.9	17.4	17.5
11	80	70.056	−126.288	12.1	48.6	18.7	16.8	16.7	16.7
12	83	70.056	−126.281	12.3	39.2	16.7	14.9	16.8	17.3
13	96	70.058	−126.29	14.4	46.6	23.7	17.7	20.8	21.4
14	99	70.039	−126.254	13.0	42.7	20.5	16.4	20.9	21.6
15	101	70.045	−126.256	13.8	58.6	23.6	17.4	21.4	21.8
16	119	70.044	−126.305	10.8	42.1	21.6	17.2	21.2	21.9

Table 3
Basic SWE statistical data calculated from rough ice snow thickness data

ID	Day	Latitude	Longitude	Transects SWE				AMSR-E SWE	
				Min	Max	Mean	SD	p-Min	p-Max
1	36	70.038	−126.26	11.4	54.9	28.1	19.3	18.7	19.3
2	54	70.048	−126.255	12.0	39.3	15.3	13.3	15.6	16.2
3	66	70.045	−126.235	11.7	59.1	22.2	19.9	14.5	14.6
4	74	70.047	−126.232	11.0	71.5	23.1	19.9	15.8	15.9
5	78	70.045	−126.251	12.2	80.3	39.0	23.0	17.2	17.6
6	97	70.036	−126.31	13.4	79.6	29.9	20.7	20.3	20.6
7	100	NA	NA	10.7	98.1	28.3	22.0	21.4	21.9
8	105	70.05	−126.25	11.4	75.7	27.3	20.3	20.3	21.2

vertical polarizations) and spatial resolution varies between 5.4 km to 56 km for 89 and 6.9 GHz respectively. The total precision varies between 0.66 to 0.68 K at 100 and 250 K respectively.

2.3.1. Atmospheric corrections

We used the daily T_b average over the ascending and descending passes since there were low diurnal variations throughout the study period. Since the SWE algorithms developed in Langlois and Barber (2007a) were based on SBR measurements (excluding atmospheric influences), atmospheric corrections were required (Tedesco and Wang, 2006). We corrected the AMSR-E brightness temperatures with regards to atmospheric contribution to T_b following Mätzler (1992). Atmospheric optical thickness values were obtained from Mätzler (1992) for Arctic regions and they fall within what was measured by Hwang, Langlois, Barber, Papakyriakou (in press) over the same region. To estimate the contribution of atmospheric temperature to the satellite, the transmissivity (Υ_{atm}) of the atmosphere was calculated such that:

$$\Upsilon_{atm} = e^{-\tau_0 \sec \theta}, \tag{1}$$

where τ_0 is the normal optical thickness and θ the incidence angle (e.g., Mätzler, 1987; Grenfell et al., 1998). Therefore, considering in-situ brightness temperature (T_b) measurements, the corresponding satellite brightness temperature ($T_{b\text{-SAT}}$) corresponds to:

$$T_{b\text{-SAT}} = (T_b \cdot \Upsilon_{atm}) + (1\text{-}e) \cdot (\Upsilon_{atm} \cdot T_{atm}\downarrow) + (1-\Upsilon_{atm}) \cdot T_{atm}\uparrow, \tag{2}$$

where $(1-\Upsilon_{atm}) \cdot T_{atm}$ is the sky brightness temperature (in both upward and downward directions). Since the emissitivity of the snow (e) is very high (usually >0.7 for 19 and 37 GHz, given frequency and polarization used), we neglected the downward T_{atm} portion that is being reflected to the satellite through the atmosphere. Thus, the corrected brightness temperature from satellite measurements can be derived from such that:

$$T_b = \frac{T_{b\text{-SAT}}-(1-\Upsilon_{atm})T_{atm}\uparrow}{\Upsilon_{atm}}. \tag{3}$$

Again, this correction needs to be applied to the satellite T_b since the SWE algorithms were developed using surface based radiometer measurements (Wang and Tedesco, 2007). However, the T_b contributions from clouds during the winter period were rather small since clear conditions were observed most of the time.

2.3.2. Sea ice roughness

In order to understand the effect of spatial features on SWE predictions, we investigated sea ice roughness using both passive and active microwave data. First, the polarization (PR) and gradient (GR) ratios from passive microwave measurements were calculated in order to explore the possibility of qualifying the 'state' of ice roughness from AMSR-E. Active microwave data were also used in combination with passive microwave data for investigating the potential impacts of roughness on the SWE predictions.

In passive microwaves, sea ice roughness can be qualified using the polarization and gradient ratios. The brightness temperatures polarization ratio (PR) is given such as:

$$PR = \frac{T_bV - T_bH}{T_bV + T_bH}, \text{ for 18.7 GHz} \tag{4}$$

where T_bV and T_bH are the brightness temperatures in the vertical (v-pol) and horizontal (h-pol) polarizations respectively. One of the main advantages in using brightness temperature polarization ratios is that they are independent of ice temperature (Cavalieri, Gloersen, and Campbell, 1984; Mäkynen and Hallikainen, 2005). The brightness temperature gradient ratio (GR) uses two different frequencies such that:

$$GR = \frac{T_bV_{f1} - T_bV_{f2}}{T_bV_{f1} + T_bV_{f2}}, \text{ where } f1 > f2. \tag{5}$$

Previous work by Mäkynen and Hallikainen (2005) had success distinguishing rough ice from new ice using both ratios. For the purpose of this study, we used 18.7 and 36.5 GHz for the GR in the vertical polarization since the largest impact of ice roughness on brightness temperatures have has been measured at these frequencies over dry snow.

Using active microwaves, a total of 36 ScanSAR (RADARSAT) Wide-B low-resolution images over the study site were analyzed between December 24th 2003 and April 30th 2004. No earlier dates were chosen because it was obvious (high backscattering values followed by low values) in the imagery that the ice had not yet consolidated and ice dynamics and open water were influencing backscatter more than surface roughness. Furthermore, images taken on days 358 and 3 showed areas of open water that influenced relative backscatter measurements (open water in Fig. 2a and smooth ice on Fig. 2b).

For each RADARSAT-1 pass, 15-by-15 and 29-by-29 pixel windows (i.e., small white boxes in Fig. 2) were centered over each of p_Min (pixel-4, with minimum averaged T_b) and p_Max (pixel-3, with maximum averaged T_b) and mean, calibrated microwave backscatter coefficient (σ°) values were extracted. A larger, 90 by 80 pixels, window was then centered over the region encompassing p_Min and p_Max from which a pool of σ° values were extracted (see large white box in Fig. 2). From this, statistical z-scores, or *normal deviates*, at both 15 by 15 and 29 by 29 pixel scales were calculated for p_Min and p_Max relative to the larger surrounding area for each RADARSAT-1 pass. This method did not explicitly address ambiguities associated with incidence angle variations throughout the time series; rather it provided an indication of the relative degree of roughness-induced σ° between the two sites, as well as relative to the larger, surrounding area. A site demonstrating a consistently higher z-score throughout the time series — irrespective of incidence angle — would be regarded as being rougher at C-band frequency, given that thermodynamically-induced changes in σ° are limited in cold conditions.

2.4. SWE algorithm

As mentioned earlier, we employed the SWE algorithms developed in Langlois and Barber (2007a) using in-situ SBR passive microwave data coupled with ancillary seasonal snow thermophysical properties. Their algorithm makes use of a multiple regression approach to retrieve SWE values with two independent variables (SWE and T_{air}) and one dependent variable (brightness temperatures, T_b). They also showed that we showed that the spectral ratio between 19 and 37 GHz cannot be applied in-situ due to very small differences observed between the two frequencies throughout the experiment. Previous research (Barber et al., 2003) used the same approach with success using the T_{si} temperature, but the best results with our dataset were obtained through T_{air} and T_{si} due to their control on temperature gradient and metamorphism which affect T_b significantly. However, using T_{air} always provided slightly better results and is also easier to retrieve from long-term datasets

Day 358   Day 24

a) Open water   b) Smooth ice
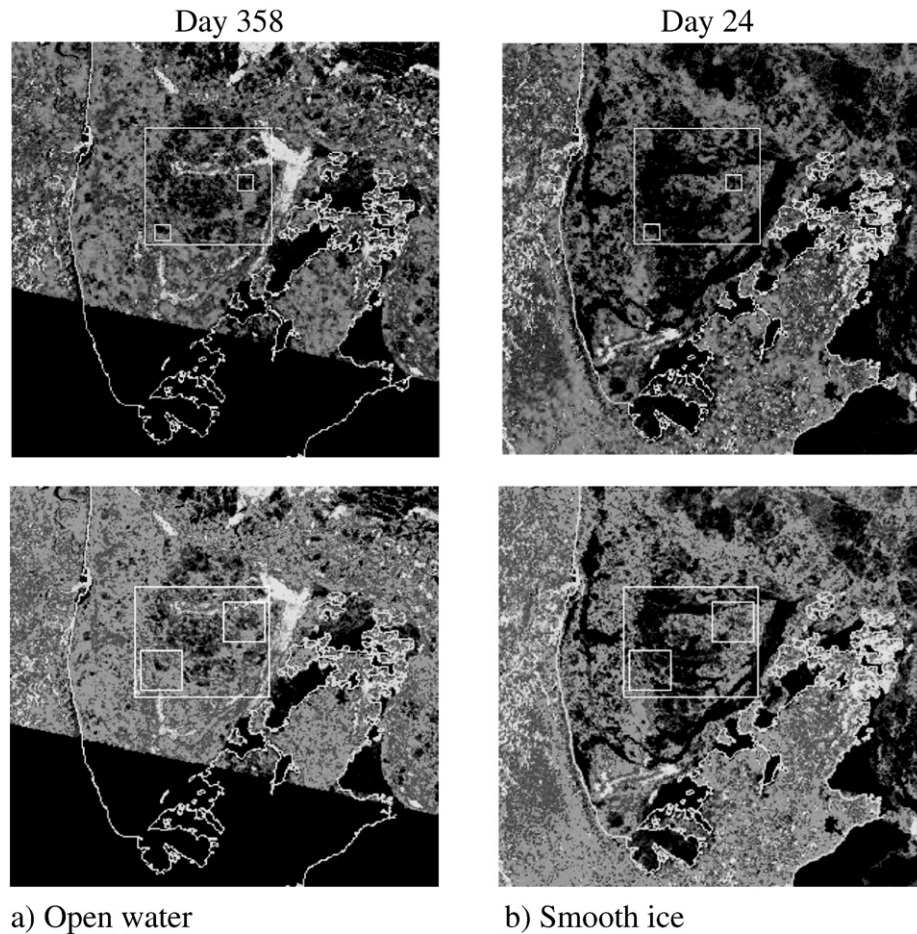
Fig. 2. ScanSAR images taken on a) day 358 and b) day 24. The top two images are at 6 km resolution, and the bottom two at 11.6 km resolution (p_Min at top right, and p_Max at bottom left).

(meteorological data, remote sensing, climate models), and easier to deal with given the spatial variation.

This algorithm adjusts for evolving snow thickness using a combination of two multiple regression-based algorithms valid over the range $-30 < T° < -5$ °C and $0 < SWE < 55$ mm given as:

$$SWE = \frac{T_{b\text{-}19V} - 0.24 T_{air} - 219.54}{2.29}, \tag{6}$$

for $0 < SWE < 33$ mm, $-30.3 < T° < -5$ °C and $246 < T_b < 288$ K and

$$SWE = \frac{T_{b\text{-}37V} + 0.01 T_{air} - 309.69}{-0.9}, \tag{7}$$

for $33 < SWE < 55$ mm, $-30.3 < T° < -5$ °C and $256 < T_b < 280$ K.

In the above equations, air temperatures are required to predict SWE and in-situ air temperatures were available through the CASES period (Langlois et al., 2007a, 2007b). For satellite remote sensing applications, we compared in-situ meteorological tower measurements with MODIS ice surface temperatures and the modeled North American Regional Reanalysis (NARR) 2-m air temperature data in order to decide which of the two products would be the most appropriate for Eqs. (6) and (7).

2.4.1. In-situ meteorological tower

The in-situ values of T_{air} were taken from a meteorological tower that was maintained on the ship throughout the CASES overwintering mission. The ship was equipped with an AXYS Automated Voluntary Observation Ship (AVOS) system on the roof of the wheelhouse away from all disturbances caused by the proximity of the ship. The AVOS system is an interactive environmental reporting system that transmitted hourly weather conditions. Temperatures (air and sea surface), pressure, wind speed, wind direction, and current GPS location were updated every 10 min and averaged daily.

2.4.2. MODIS

MODIS/Aqua Daily L3 Global 4 km EASE-Grid ice surface 'skin' temperatures (IST) were retrieved for the AMSR-E pixels. We averaged the temperatures values of 3×3 pixels encompassed within each AMSR-E pixel. The MODIS data algorithm uses a Normalized Difference Snow Index (NDSI) modified for sea ice to distinguish sea ice from open ocean based on reflective and thermal characteristics (Hall, Riggs, Salomonson, 2007). The ice surface temperature data are expressed in Kelvin using calibration data. The algorithm assumes that sea ice is snow covered and that snow dominates the reflectance characteristics. Furthermore, a cloud mask algorithm distinguishes clouds from ice in the output product (Hall, Solberg, Riggs, 2004). Accuracy of IST is estimated to be 0.3 to 2.1 K over the 245-270 K range for all ice types (Key, Collins, Fowler, Stone, 1997). MODIS Airborne Simulator (MAS) data and campaign field data are currently used to establish bounds for MODIS IST accuracy. We also retrieved the average temperatures over a 3200 km² area within Franklin Bay (average over 10×20 pixels at 4 km resolution).

2.4.3. North American Regional Reanalysis (NARR)

Finally, we extracted 2-m air temperatures from the North American Regional Reanalysis (NARR) from the National Centers for

Environmental Prediction (NCEP) Environmental Modeling Center (EMC). We used daily average values from 9 pixels (3×3 at 32 km resolution) located within Franklin Bay and Amundsen Gulf encompassing AMSR-E and MODIS pixels. The horizontal resolution is 0.3° on the Eta AWIP grid and the temporal resolution is 8 times daily (every 3 h) and averaged over a 24-hour period.

3. Results and discussion

3.1. Air temperatures

The in-situ air temperatures from the meteorological tower followed a typical seasonal evolution pattern with a cooling period (days 343–59) and a warming period (days 60–122). Values between days 343 and 59 decreased slightly, then reached a minimum daily average value of −36.24 °C (Fig. 3a). The largest variations were measured on days 357, 5 and 29 where temperatures peaked to −13.1, −1.23 and −17 °C respectively. Smaller variations were observed during the warming period with the exception of one significant increase between days 85 and 101 in the order of approximately +1 °C day^{-1}. Daily MODIS ice surface temperatures were only available for day 14 onward (Fig. 3a). The minimum temperatures were reached on day 67 at −36.15 °C and increased afterwards until the end of the sampling period on day 122. Maximum temperatures were measured on day 101 at −10.28 °C, and

the warming rate between day 67 and day 122 was approximately 0.5 °C day^{-1}. Daily NARR 2-m air temperature data are depicted in Fig. 3a. These data were available for the entire study period from day 343 and 122. Air temperature values decreased between day 343 and 41 where the seasonal minimum was reached for the region at −33.4 °C.

Overall, the temperatures from the meteorological tower agreed quite well with MODIS ice surface temperatures (assumed to be equal to air temperature) with a R^2 of 0.82 and an average error of +0.29 °C (Fig. 3b). There are no particular temporal trends in the error where the largest overestimation occurred on day 41 (+9.38 °C) and the largest underestimation was on day 29 (−7.07 °C). NARR data also correlated well with the meteorological tower measurements with a R^2 of 0.61. The error from the NARR data underestimated air temperatures until day 18, whereas it overestimated slightly the values for the remaining period. The maximum error measured was +10.6 °C on day 89 and a minimum of −13.7 °C on day 14. However, since MODIS data contains gaps in the time series due to cloud cover, we suggest using NARR air temperature data in Eqs. (6) and (7) since the temporal coverage is better.

3.2. AMSR-E brightness temperatures

The atmospherically corrected brightness temperatures difference between the ascending and descending passes was negligible (no diurnal effects). Therefore, we used the daily average T_b measurements
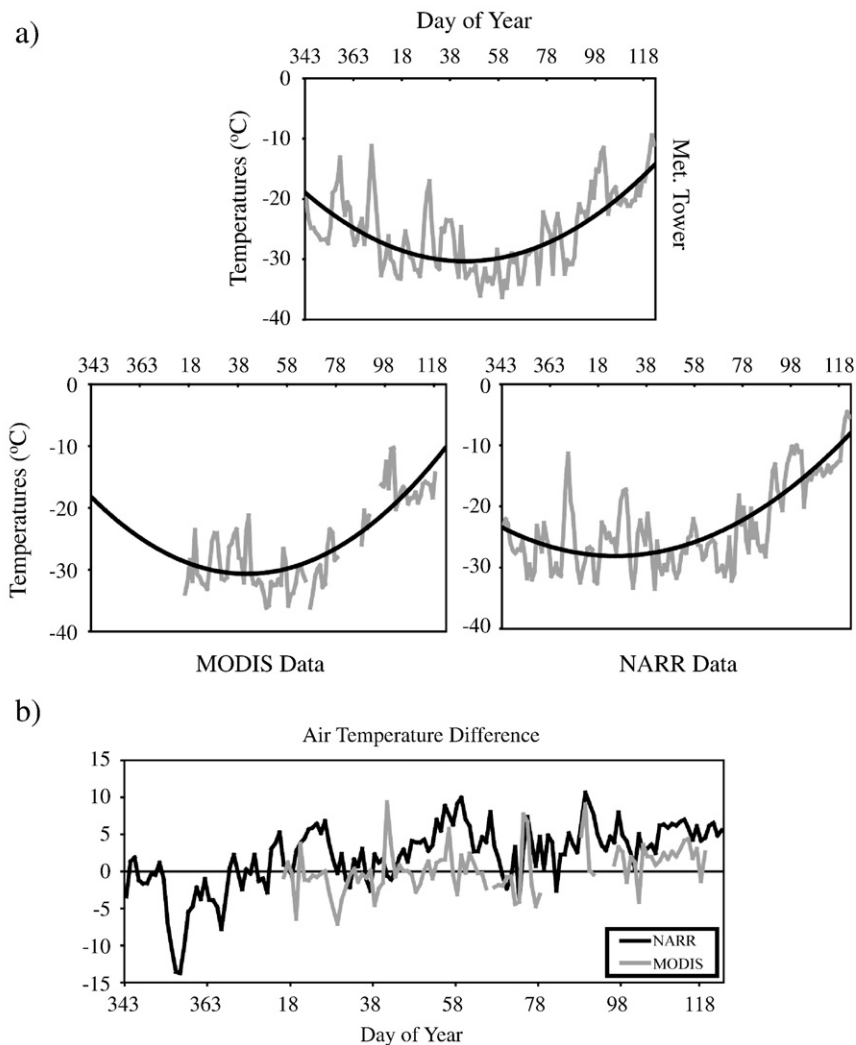

Fig. 3. Temporal evolution of a) meteorological tower, MODIS and NARR air temperatures and b) the differences between MODIS and NARR data with respect to the meteorological tower (considered as reference).
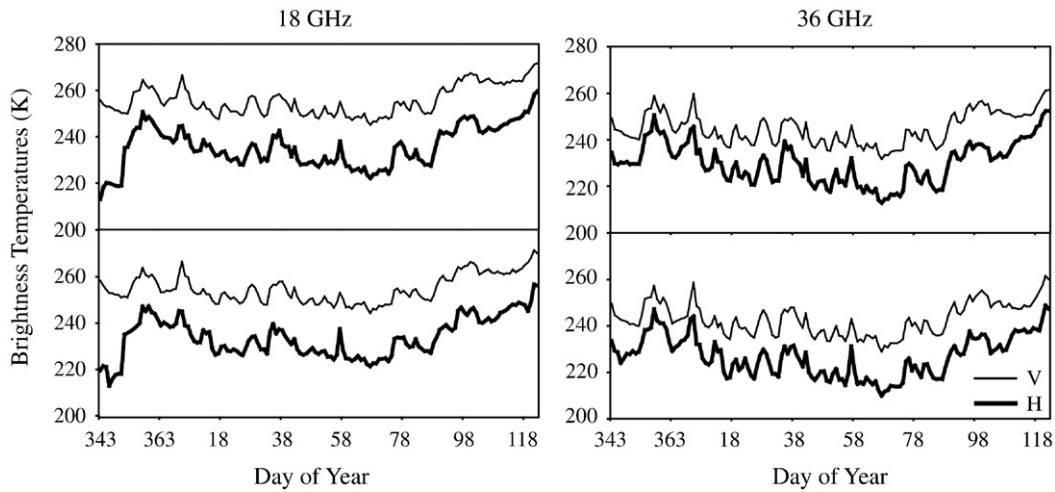
Fig. 4. Temporal evolution of atmospherically corrected AMSR-E brightness temperatures in both vertical and horizontal polarizations.

for the SWE algorithm application. The brightness temperature values did not vary much throughout the bay from pixel to pixel (spatial variability). The atmospherically corrected brightness temperatures for both 18.7 and 36.5 GHz in h-pol and v-pol are depicted on Fig. 4 for p_Min and p_Max (pixels 3 and 4 from Fig. 1). The brightness temperatures at 36.5 GHz varied slightly more than 18.7 GHz with small differences between the pixels (Fig. 4). Overall, a strong increase was measured early during the sampling period at 18.7 GHz in the h-pol whereas a general decrease was observed until day 67 where the minimal seasonal values were reached at both 18.7 and 36.5 GHz.

3.3. SWE predictions

Predicted snow water equivalent data using air temperatures from the NARR re-analysis and AMSR-E brightness temperatures are depicted in Fig. 5. Overall, the SWE values oscillated between 15 and 25 mm. Three major depositional events occurred around days 5, 42 and 91 (circled in Fig. 5). We assume that AMSR-E responded to those depositional (precipitations) events and other peaks in predicted SWE values could be due to blowing snow that redistributes snow thickness without necessarily needing precipitations. For instance, the peaks in SWE predicted on days 19, 29, 52 and 82 corresponded to daily averaged wind speed over 10 m s^{-1}. However, it is hard to conclude whether blowing snow is significant over a satellite footprint, particularly when two adjacent footprints give essentially the same result (e.g. Fig. 7). The total snow mass averaged over a large homogeneous area is not changed much by blowing it around, but density would increase. The effect could also be related to the alteration of the vertical temperature gradients and the horizontal temperature contrast of the surface produced by strong wind. Even though no statistical analysis was conducted due to a lack of in-situ SWE measurements, an extended look at wind data and predicted SWE values showed that the predictions could potentially be affected by blowing snow. Results showed that all wind events where daily average wind speed exceeded 10 m s^{-1} were associated with an increase in predicted SWE. In a total of 10 events, all showed an increase in SWE, however the amplitude of the increase were was quite variable (from approximately 0.5 mm to 4 mm). The amplitude of the daily variations decreased between day 343 and day 70 and predicted values generally increased between days 78 and the end of the sampling period, although no relationships were established between those variations and blowing snow events. Maximum seasonal values were recorded at the end of the sampling period at 23.3 and 23 mm for p_Min and p_Max respectively. Again, the overall difference between the two pixels was very small with an average of 0.3 mm and a maximum of 1.2 mm.

The algorithm is not sensitive to large variations in air temperature since the SWE variations are much smaller than air temperatures variations. Specifically, an increase of 5 °C in Eq. (6) corresponds to an offset of 0.52 mm whereas a much smaller value is measured in Eq. (7) at 0.08 mm. Therefore, the thicker the snow gets, the less sensitive the algorithm is to air temperature variations. Furthermore, brightness temperatures from AMSR-E remained between 244 and 271 K, within the range of validity for the algorithm. However, the SWE values did not increase over the 33 mm threshold identified in Langlois and Barber (2007a) since predictions from p_Min and p_Max remained between 14 and 23 mm (no switch from Eq. (6) to Eq. (7)). The details of this result will be discussed later.

Hence, we compared the SWE predictions from Eq. (6) for both p_Min and p_Max with in-situ snow water equivalent (SWE) transects collected over smooth and rough ice within the AMSR-E pixels (Tables 2 and 3). In what follows, we provide a comparison between measured and predicted SWE values for both smooth and rough ice environments.

3.3.1. Smooth ice snow water equivalent data

Basic statistical data (minimum, maximum, mean and standard deviation) for all smooth SWE transects are depicted in Table 2. We found that the SWE predictions are statistically significant with the measured smooth ice SWE values within +/−1 standard deviation of the measured in-situ values from Table 2 (Fig. 6). A strong correlation was found between predicted and measured data with R^2 values of 0.75 and 0.73 in p_Min and p_Max respectively. The measured SWE standard deviation increased throughout the study as shown in Table 2 and Fig. 6, which can be explained by higher spatial variations in snow thickness as
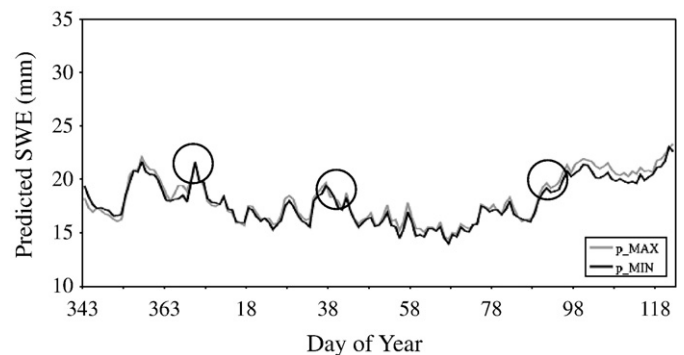

Fig. 5. Temporal evolution of predicted SWE using air temperature data from the NARR re-analysis and AMSR-E brightness temperatures.
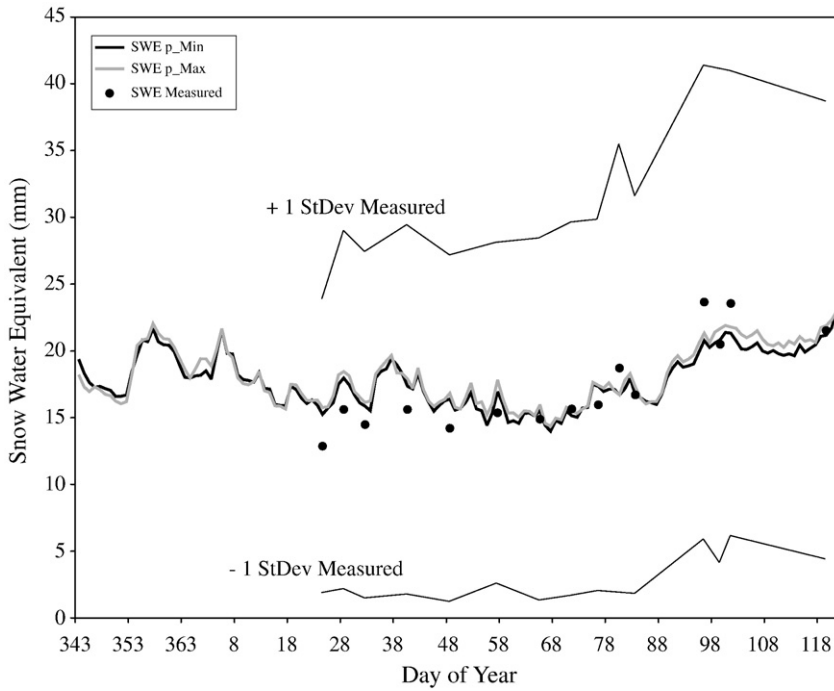
Fig. 6. Temporal evolution of SWE predictions for modeled p_Min and p_Max (black and gray lines), and measured at the smooth SWE transects sites (dots).

snow thickens (Iacozza and Barber, 2001). Measured SWE over smooth ice increased from an average of 15 mm (prior to day 65) to 19.1 mm (after day 65) whereas the predicted SWE increased from 16.8 mm to 18.6 mm combining both p_Min and p_Max (Table 2). The differences between predicted and modeled values were on average 1.5 and 1.7 mm for both p_Min and p_Max respectively.

3.3.2. Rough ice snow water equivalent data

Basic statistical data (minimum, maximum, mean and standard deviation) for all rough ice SWE transects are depicted in Table 3. We also found the SWE predictions to be statistically significant within +/−1

standard deviation of the measured SWE values over rough ice, although predictions are not as strong as measured over smooth ice. The measured roughness elevation varied between 15 and 140 cm on average including snow thickness, which generally increased as the season progressed.

The temporal evolution of the measured SWE over rough ice did not follow any particular trend, although higher values were recorded towards the end of the sampling period (Table 3 and Fig. 7). The algorithm generally underestimated SWE by −8.7 and −8.2 mm for p_Min and p_Max respectively (Fig. 7). The largest difference was measured on day 78, where the average measured SWE value was
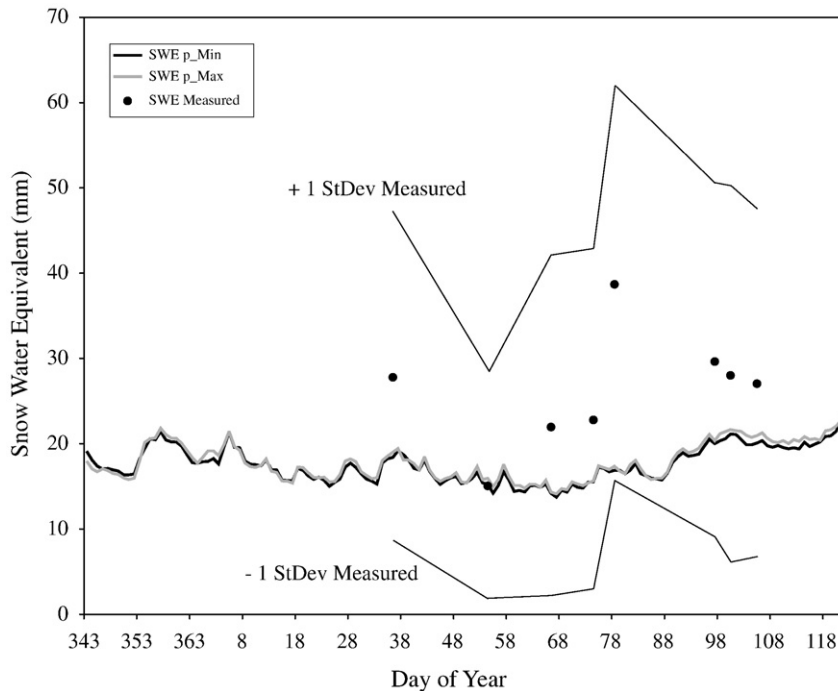

Fig. 7. Temporal evolution of SWE predictions for modeled p_Min and p_Max, and measured at the rough snow thickness transects sites.

39 mm (difference of approximately 22 mm with the predicted values), by far the highest value recorded throughout the study period. If we exclude this SWE transect from the average, the underestimation decreased to −6.8 and −6.3 mm for p_Min and p_Max respectively.

We mentioned earlier that the algorithm did not switch from thin to thick snow. Hence, one may think that the thick snow algorithm should be applied in rougher ice since thicker snow is found given Table 3 due to snow catchments by the ice ridges (e.g., Granberg, 1998). Hence, we applied the thick snow algorithm from Eq. (7) to see if better predictions would be found in Fig. 7 in rougher ice. Results showed that predictions were too high with SWE values of approximately 60 mm for both p_Min and p_Max. This can be explained by the differences measured between the SBR brightness temperatures (over which the algorithm was developed) and the brightness temperatures from AMSR-E. The comparison of both sets of T_b values showed that the brightness temperatures measured by the SBR were higher during the winter resulting in lower SWE predictions using Eq. (6). On average, the SBR T_b at 36.5 GHz Eq. (7) were was 35 K higher than measured with AMSR-E. The difference was smaller at 18.7 GHz, which is used in the thin snow algorithm Eq. (6) explaining the better results found using this algorithm. Furthermore, it was demonstrated in various studies that thick snow thermodynamic processes such as volume scattering and brine volume migration governed microwave emission at the SBR scale over smooth ice during the winter period (Langlois and Barber, 2007a). Those processes are not dominant in a rough ice environment which might explain the

better predictions obtained over smooth ice. Unfortunately, we did not carry out an experiment with the SBR over rough ice, and this should be a priority in future work.

Also, it was showed in Mäkynen and Hallikainen (2005) that T_b decreases with increasing ice deformation at 18.7 and 36.5 GHz in the vertical polarization (used in Eqs. (6) and (7)) over a partial (mix of bare ice and snow) dry snow cover typically found in rough ice. This situation was found in the study area (i.e. AMSR-E scale), although not in the SBR field of view. Hence, decrease in T_b due to ice roughness was not measured by the SBR over smooth ice (totally covered by snow), which was also observed by Mäkynen and Hallikainen (2005). A decrease in T_b measured by AMSR-E through ice roughness will increase SWE predictions using Eq. (7). More specifically, an increase in the order of 35 K (measured average difference at 36.5 GHz between days 343 and 57), would decrease SWE values by approximately 40 mm. Therefore, a correction should be applied to AMSR-E brightness temperatures if one wants to apply the thick snow algorithm over Eq. (7) a rough ice environments.

Limited SWE data were available in rough ice, and limited roughness amplitudes (all rough transects conducted in average roughness heights between 111 and 157 cm) were sampled. However, to test this roughness hypothesis, we simply corrected the AMSR-E brightness temperatures so that they match SBR measurements during the C2 and C3 periods. By doing so, we found the SWE predictions from Eq. (7) to vary between 31 and 42 mm, +/−2.5 mm for both p_Min and p_Max respectively. This represents a much better result given Fig. 7, when compared to the 60–
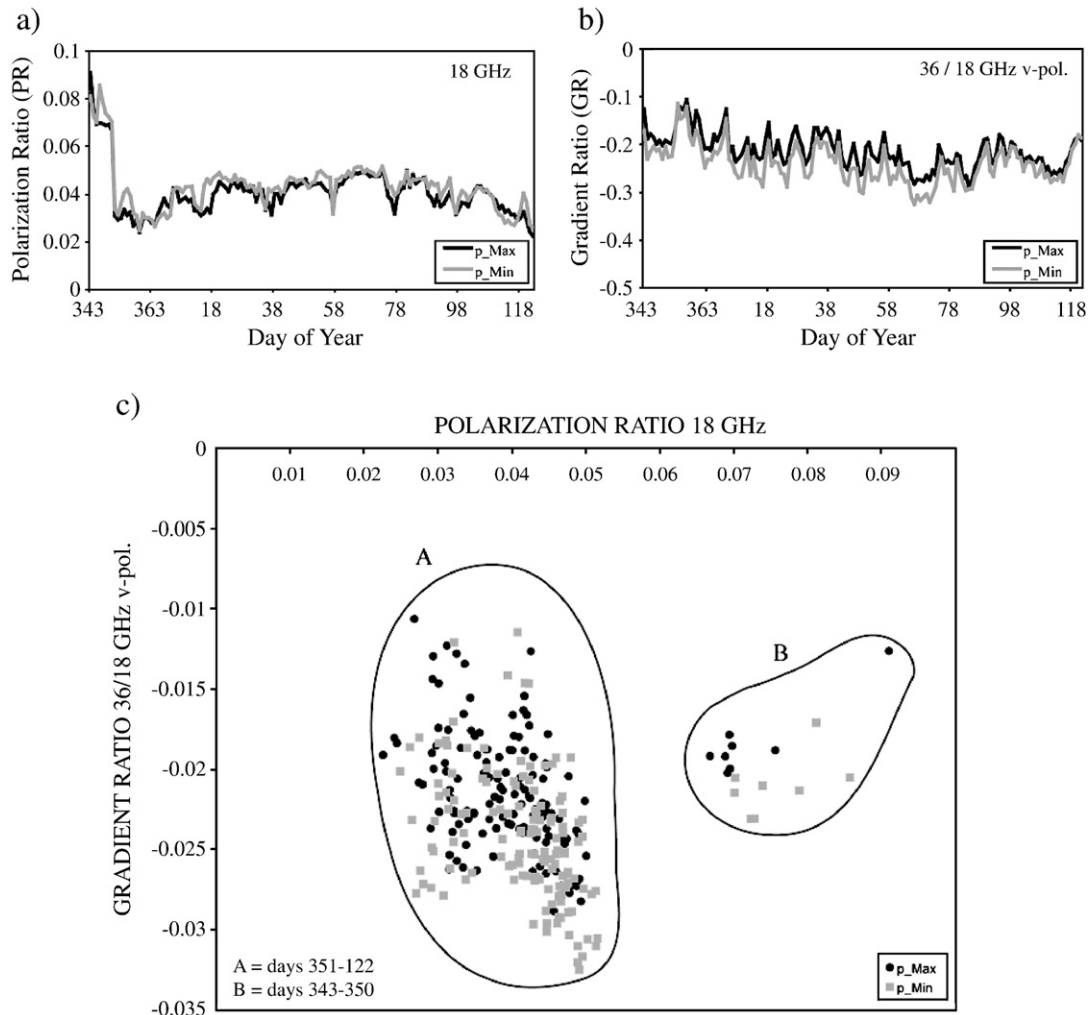
Fig. 8. Temporal evolution of a) polarization ratio at 18.7 GHz and b) the gradient ratio between 18.7 and 36.5 GHz for both p_Min and p_Max. In c) a scatter plot of the polarization ratio and gradient ratio.

80 mm predictions without correcting the initial T_b for Eq. (7). However, more data over a wider range of snow thickness and ice roughness would be required to develop statistically viable corrections to Eq. (7) for rough ice applications.

This simple modification on brightness temperatures confirms that a certain degree of correction is required when using the thick snow algorithm over rough ice. Although atmospheric corrections were conducted, it appears that the scale difference between the SBR and AMSR-E can be a significant factor due to the different dynamic and thermodynamic processes (highlighted in Langlois and Barber, 2007b) affecting both scales at different amplitudes. Since no SBR measurements occurred over rough ice, we could not develop nor modify the existing algorithm even though it appears that a certain degree of correction would greatly enhance prediction results. Furthermore, the fraction and amplitude of ice roughness within one AMSR-E pixel should be analyzed, but a lot of uncertainties remain on how to do so from a satellite perspective. In what follows, we provide insight as to where future roughness analysis should go in order to first qualify and quantify ice roughness using a combination of passive and active microwave satellite information for SWE prediction applications.

3.4. Roughness analysis

As shown in the previous section, ice roughness can alter SWE predictions where the algorithm underestimates SWE values in rough ice, although still significant within +/−1 standard deviation from the measured data (Fig. 7). Hence, the state of roughness in both p_Min and p_Max needs to be addressed from a satellite perspective. The effect of roughness on the SWE predictions will be discussed later.

3.4.1. Impact of roughness on passive microwaves

As previously discussed, the polarization ratio (PR) was calculated at 18.7 GHz for both pixels using Eq. (4). A sharp decrease in PR was measured from 0.91 on day 343 to 0.294 on day 352 for p_Max (Fig. 8a) whereas it decreased from 0.812 to 0.315 at p_Min. Values increased slightly afterwards until days 67–68 and decreased again until the end of the sampling period. The gradient ratio (GR) at 18.7 and 36.5 GHz values decreased slightly throughout the study period (Fig. 8b). Values were at maximum early on day 354 for p_Min (−0.0106) and 357 for p_Max (−0.0115). The minimum was reached on days 67 and 85 for p_Min and p_Max respectively (−0.0325 and −0.0288). A plot of GR against PR is given in Fig. 8c. Two statistically distinct clusters arise (A and B) where A are PR and GR values from day 351 to 122 and B values prior to day 351 (343–351).

It was found in Mäkynen and Hallikainen (2005) that as surface roughness increases, dry snow brightness temperatures decreases in the vertical polarization, whereas values in the horizontal polarization did not change as significantly (i.e., decrease in PR with increasing ice roughness). From their conclusions, Fig. 8 could suggest that a transition from new ice to rough ice was observed within our AMSR-E pixels early in the season, but it could also be due to an open water to new ice transition which would also decrease the PR values (Fig. 8a). Open water is reflective in microwave bands and has a very strong polarization effect ($T_bV \gg T_bH$) compared to first-year sea ice (Fig. 8a).

In order to find evidence of open water between days 343 and 3 where a large decrease in PR was measured, we looked at ice charts from the Canadian Ice Service (CIS). On January 1st, all of Franklin Bay was considered as fast ice, however, no information was available prior to that. Hence, we extracted sea ice concentration (SIC) values from the
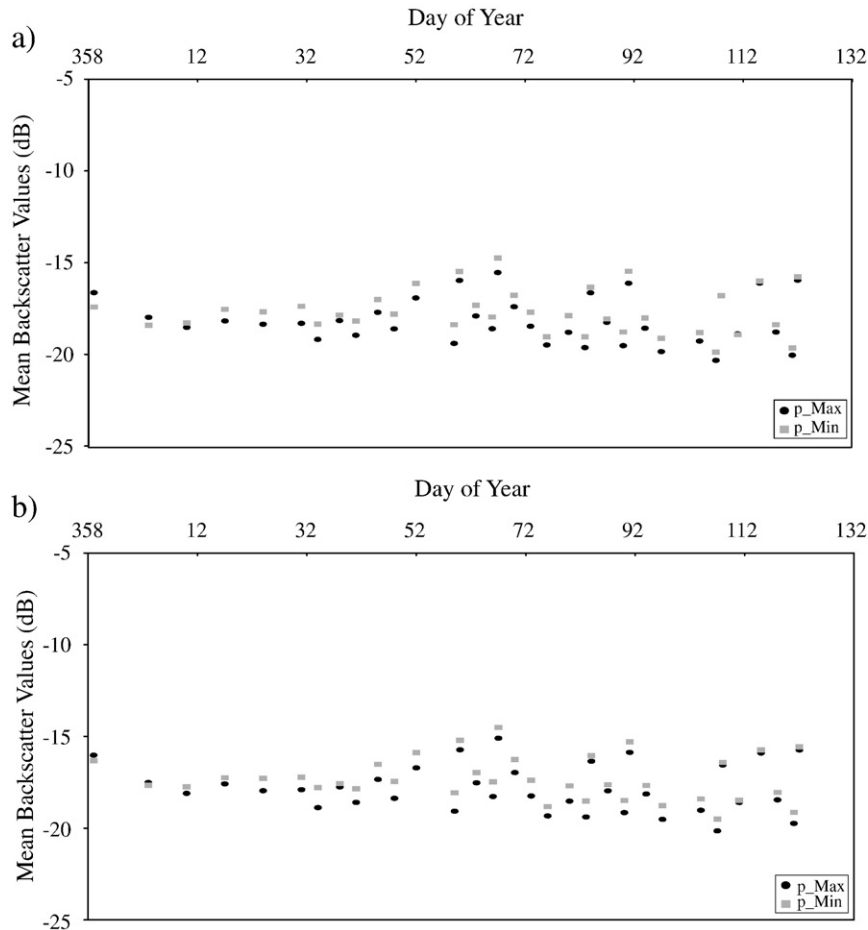

Fig. 9. Mean backscatter values for p_Min and p_Max at a) 6 km and b) 11.6 km of resolution.

AMSR-E algorithm (Markus and Cavalieri, 2000) to examine any evidence of open water detected over the same period. Sea ice concentration results extracted from p_Min and p_Max did not provide any evidence of open water since ice concentration varied from 98 to 100% between days 343 and 3, in agreement with the CIS ice charts. Furthermore, we extracted SIC from 12 pixels within Franklin Bay for the same period, and results were similar throughout the bay suggesting that the ice was consolidated at AMSR-E scales on day 343. However, given the results presented in Fig. 8, open water was most likely present in the early stages of the sampling period, although its fraction was probably sufficiently small so that both CIS charts and AMSR-E SIC algorithm considered the region as fast ice. For further insight regarding p_Min and p_Max spatial features temporal evolution (ice roughness, open water etc.), we looked at active microwave satellite data which might help understand the results presented above.

3.4.2. Impact of roughness on active microwaves

Mean backscatter values were analyzed at 6 and 11.6 km resolutions, centered on the AMSR-E p_Min and p_Max pixels to evaluate the scaling effect on $\sigma°$ in both p_Min and p_Max (Fig. 2) and provide further information on sea ice roughness. Throughout the study period, mean $\sigma°$ values at 6 km resolution within p_Min were consistently higher than p_Max. Backscatter values did not follow any particular trend throughout the study period oscillating between −15 and −20 dB. The maximum was recorded on day 66 where $\sigma°$ reached −14.7 and −15.5 dB and minimum on day 106 at −19.9 and −20.3 dB for both p_Min and p_Max respectively (Fig. 9a). This appears to be irrespective of incidence angle, as it is fairly consistent from about day 10 to day 107. Overall, $\sigma°$ prior to day 48 did not vary greatly whereas the maximum variations were measured between days 66 and 75. Results at 11.6 km showed the same temporal behavior with maximum (−14.5 and −15.1 dB) and minimum (−19.5 and −20.2 dB) $\sigma°$ measured on day 66 and 106 for

p_Min and p_Max respectively (Fig. 9b). The differences between both scales are minimal with slightly higher $\sigma°$ values measured at 11.6 km. On average, values were higher of 0.33 and 0.38 dB in p_Max and p_Min respectively. The largest differences between the two scales were measured on day 358 (Fig. 9).

Furthermore, z-scores from Fig. 10 show that both p_Min and p_Max were rougher (higher backscatter values) relative to the surrounding areas (i.e., the larger pixel window from Fig. 8) and that p_Min is consistently rougher at both 6 km on Fig. 10a and 11.6 km on Fig. 10b. From day 10 to day 106, p_Max backscatter was on average 0.15 standard deviations above the mean of the larger pixel window whereas p_Min reached 0.43 standard deviations above the mean of the larger pixel window (Fig. 10). That value increased to 0.2 and 0.49 at 11.6 km for both p_Max and p_Min respectively. While p_Min and p_Max both represent smooth first-year sea ice (FYI), in a relative sense they both exhibit above average roughness for the FYI in this region.

Mäkynen and Hallikainen (2004) reported an increase in $\sigma°$ with increasing ice roughness. The increase was in the order of 10 dB in both co- and cross polarizations at 23° and 45° of incidence angle from new ice to highly deformed ice. Once the ice was in place, we did measure an increase in $\sigma°$ between days 12 and 65, however the increase was in the order of approximately +5 dB. It is well known that SAR $\sigma°$ measurements are very sensitive to small small-scale roughness (i.e., on the order of 1/10 the incident radar wavelength, λ), but it is also sensitive to changes in the orientation of small-scale scatterers induced by larger scale roughness features (e.g., Manninen, 1992; Livingstone, 1994; Yackel, Barber, Papakyriakou, 2001; Yackel and Barber, 2007). Using $\sigma°$ to strictly quantify 'roughness' becomes a problem given that roughness can be thought of as a relative term that is associated with the distribution of scatterers at multiple scales (e.g., mm-scale ice roughness superimposed upon larger cm-scale ice blocks). Additional fluctuations in $\sigma°$ during winter could be caused by
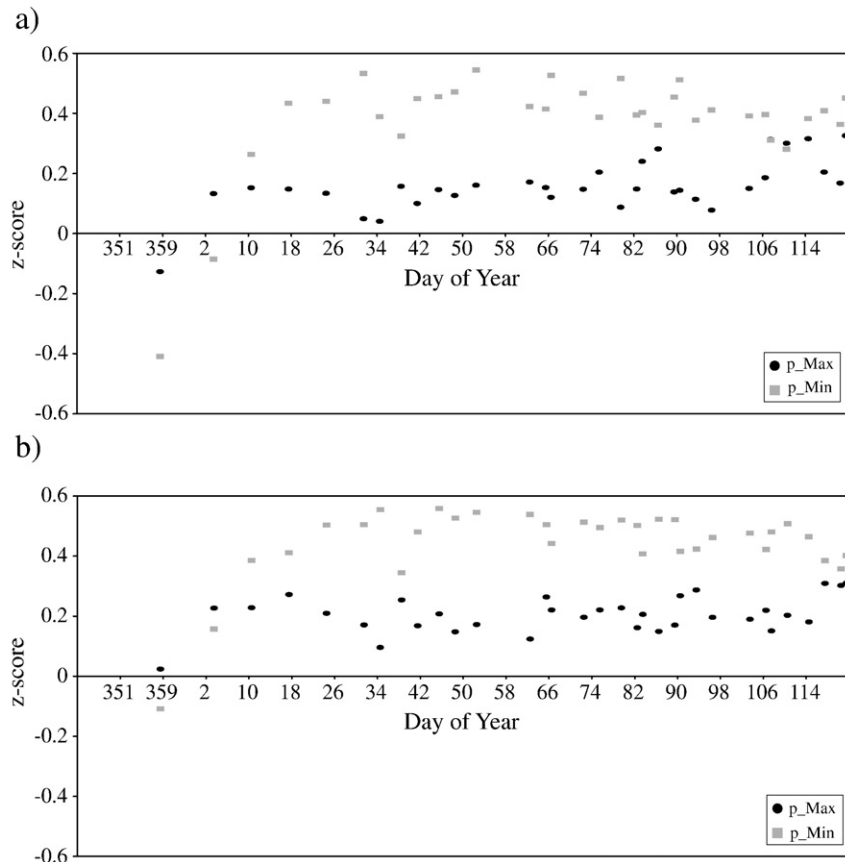

Fig. 10. Standardized backscatter values for both p_Min and p_Max relative to the surrounding area at a) 6 km and b) 11.6 km resolutions.

either changes in snow and ice thermodynamic processes and related thermophysical properties, or changes in small small-scale surface roughness (e.g., Barber and Thomas, 1998; Barber and Nghiem, 1999; Nghiem and Bertoia, 2001).

From the SAR analysis, we were unable to quantify roughness in terms of amplitude. We found that the two pixels analyzed are likely rougher than what is found elsewhere in the bay. Since the brightness temperatures were very stable throughout Franklin Bay, we speculate that the amplitude of roughness variations from one pixel to another did not significantly affect brightness temperatures (i.e. SWE predictions). However, we found that the algorithm underestimated SWE in areas of rough ice (Fig. 7), but no quantification of the fraction of roughness within one AMSR-E pixel could be determined.

Results also showed that absolute and relative σ° were consistently different between p_Min and p_Max. Backscatter results between days 358 and 3 do not show evidence of open to new ice transition, although open water was present elsewhere in the area (bright areas Fig. 2a). At 11.6 km, we noticed that the analyzed window is fairly close to this zone of open water (North East of p_Min and South West of p_Max) which might explain its effect on AMSR-E 12.5 km pixel (Fig. 8). Hence, open water was most likely present within the AMSR-E pixels, although its fraction was not large enough to have a significant impact on the SIC algorithm and the CIS ice charts.

4. Conclusions

4.1. Scaling effects on SWE predictions

Looking at our SWE predictions temporal evolution, we examined how sensitive the SWE predictions were to variations in PR during the open water to new ice transition around day 350. No apparent relationship between the PR decrease and SWE prediction was found, and more work is required due to the limited data available. It is well known that open water strongly influences T_b values and existing spaceborne SWE algorithms already consider the fraction of open water within one pixel (Markus et al., 2006). Furthermore, the scaling effect was obvious when comparing the SBR T_b with the T_b measured from AMSR-E in this paper. Using Eq. (6), a lower brightness temperature means a lower predicted SWE value, which could explain the difficulty of the algorithm to increase SWE in a rough ice environment. We showed that the use of the thick snow algorithm provides much better results, although a level of correction was required. This suggests that a 'corrected' thick snow algorithm should be applied even though calculated SWE values did not reach the threshold identified in Langlois and Barber, 2007a at 33 mm (or a different threshold should be found for AMSR-E). However, the data presented are not sufficient to provide an exact correction to be applied on the AMSR-E T_b. It might be advisable to explore the possibility of using 18.7 GHz as well for thick SWE retrievals (in Eq. (7)) since we showed that the difference between SBR and AMSR-E T_b is smaller at this frequency. However, more field data are required to develop, compare and test such an algorithm.

4.2. Ice roughness vs passive and active microwaves

From the passive and active microwave data analysis conducted in this paper, it is hard to conclude on which of the two pixels is the roughest. Within a satellite footprint, spatial heterogeneity is quite important as it is not likely to contain 100% snow cover throughout the pixel, but rather a mix of a snow, bare ice, ice ridges and open water. In such case, previous research showed that rough pixels will 1) decrease the brightness temperatures in the vertical polarization, 2) decrease the polarization ratio and 3) increase σ° values. From the results presented in this paper, it appears that p_Min would be the roughest pixel since the brightness temperatures are lower and backscattering measurements higher once the ice was consolidated.

4.3. Future work

We showed that the predictions over smooth ice were very good, and results over rough ice (using a certain level of correction) are promising. The question remains: How do we quantify roughness within one AMSR-E pixel? That question is still unanswered in a precise manner as the fractions of smooth vs rough ice within p_Min and p_Max are still unknown, but we see the coupling between passive and active microwave essential in answering this question. We are confident in the large large-scale application of the algorithm as is for smooth ice, and current work over rough ice is being conducted in our lab.

Precisely, a target for a level of tolerance as to what fraction and amplitude of roughness is appropriate for the SWE from Eqs. (6) and (7) should also be identified and extended large-scale in-situ validation is required. Hence, it appears that the SWE predictions will not be significantly affected by a certain level of ice roughness (up to 140 cm as measured in the SWE transects) given that the pixels were 'rougher' than average (Fig. 10a and b), but the spatial fraction of roughness within the AMSR-E pixel still needs to be addressed. Also, it was showed that a degree of sensitivity to blowing snow exists (with wind > 10 m s^{-1}) due to changes in the spatial distribution of snow thickness. However, more work is required to increase the amount of in-situ data after blowing snow events in order to understand the role of roughness in such conditions with regards to spatial redistribution of snow thickness. SWE transects should be conducted in various wind conditions over smooth and rough ice to quantify the impact on the predictions for different rates of wind speed associated with the different transport mechanisms.

Hence, results presented in this paper provide guidance to further research that should be conducted on the subject. Some of the limitations discussed above should be addressed in future research. The main limitation of this paper is the absence of video data to support the roughness analysis. Even though we conducted video flights in the region during the study, the lines are still a small representation of the AMSR-E pixel, therefore would not add any other significant information. Therefore, a coupling between airborne passive microwave and video recording at all in-situ/airborne/satellite scales will be required to understand the true effect of roughness on brightness temperatures. The next intuitive step is then to look relating different winter scenes (PMW and SAR) through a spatial analysis of roughness and polarization ratio using the airborne data as suggested above. Obviously, in-situ measurements of snow and sea ice thermophysical properties should be conducted coincidently given the usual financial and logistical constraints of Arctic research. Even though recent SWE studies are promising, lingering uncertainties remained with regards to spatial variability. We need to be able to quantitatively determine the effect of different fractions of various spatial features on T_b in order to accurately understand the potential effects on SWE predictions. Given the importance of snow in the Arctic's system, those issues should be prioritized in future research, and eventually feed in GCMs, that still have strong assumptions with regards to snow.

References

Barber, D. G., Iacozza, J., & Walker, A. (2003). Estimation of snow water equivalent using microwave radiometry over Arctic first-year sea ice. *Hydrological Processes, 17*, 3503–3517.

Barber, D. G., & Nghiem, S. V. (1999). The role of snow on the thermal dependence of microwave backscatter over sea ice. *Journal of Geophysical Research*, *104* 25,789-25,803.

Barber, D. G., & Thomas, A. (1998). The influence of cloud cover on the radiation budget, physical properties and microwave scattering coefficient of first-year and multiyear sea ice. *IEEE Transactions on Geoscience and Remote Sensing*, *36*, 38–50.

Cavalieri, D., & Comiso, J. (2004). *Updated daily AMSR-E/Aqua Daily L3 12.5 km Tb, Sea Ice Conc., and Snow Depth Polar Grids V001, March to June 2004.* CO, USA: Boulder National Snow and Ice Data Center. Digital media.

Cavalieri, D. J., Gloersen, P., & Campbell, W. J. (1984). Determination of sea ice parameters with the NIMBUS-7 SMMR. *Journal of Geophysical Research*, *89*, 5355–5369.

Chang, A. T. C., Foster, J. L., & Hall, D. K. (1987). Nimbus-7 derived global snow cover parameters. *Annals of Glaciology*, *9*, 39–44.

Cordisco, E., Prigent, C., & Aires, F. (2006). Snow characterization at a global scale with passive microwave satellite observations. *Journal of Geophysical Research*, *111*. doi:10.1029/2005JD006773 D19102.

Eiken, H. (2003). From the microscopic, to the macroscopic, to the regional scale: Growth, microstructure and properties of sea ice. In D. N. Thomas, & G. S. Dieckmann (Eds.), *Sea Ice: An Introduction to its Physics, Chemistry, biology and Geology* (pp. 22–81). Oxford, UK: Blackwell Science Ltd.

Eppler, D. T. (1992). Passive microwave signatures of sea ice. In Frank Carsey (Ed.), *Chapt 4, Microwave remote sensing of sea ice* (pp. 47–71). Washington, D.C.: American Geophysical Union.

Foster, J. L., Sun, C., Walker, J. P., Kelly, R., Chang, A., Dong, J., & Powell, H. (2005). Quantifying the uncertainty in passive microwave snow water equivalent observations. *Remote Sensing of Environment*, *94*, 187–203.

Francis, J. A., Hunter, E., Key, J. R., & Wang, X. (2005). Clues to variability in Arctic minimum sea ice extent. *Geophysical Research Letters*, *32* L21501, 4 pages.

Garrity, C. (1992). Characterization of snow on floating ice and case studies of brightness temperature changes during the onset of melt. In F. Carsey (Ed.), *Microwave remote sensing of sea ice* (pp. 313–328). Washington, D.C.: American Geophysical Union.

Granberg, H. (1998). Physics of ice-covered seas, vol. 2. *Lecture notes from a summer school in Savonlinna* (pp. 605–649).

Grenfell, T. C., Barber, D. G., Fung, A. K., Gow, A. J., Jezek, K. C., Knapp, E. J., Nghiem, S. V., Onstott, R. G., Perovich, D. K., Roesler, C. S., Swift, C. T., & Tanis, F. (1998). Evolution of electromagnetic signatures of sea ice from initial formation to the establishment of thick first-year ice. *IEEE Transactions on Geoscience and Remote Sensing*, *39*, 13 pages.

Hall, D. K., Riggs, G. A., & Salomonson, V. V. (2007). *Updated daily. MODIS/Aqua snow cover daily L3 global 0.05 deg CMG V005, [December 2003–May 2004].* Colorado USA: Boulder National Snow and Ice Data Center. Digital media.

Hall, D. K., Solberg, R., & Riggs, G. A. (2004). Sea ice surface temperature product from MODIS. *IEEE Transactions on Geoscience and Remote Sensing*, *42*, 1076–1087.

Hwang, B.J., Langlois, A., Barber, D.G. and Papakyriakou, T.N. (in press), Detection of the thermophysical state of landfast first-year sea ice using in-situ microwave emission during spring melt. Remote Sensing of Environment, RSE-D-06-00435R2.

Iacozza, J., & Barber, D. G. (2001). Ablation patterns of snow cover over smooth first-year sea ice in the Canadian Arctic. *Hydrological Processes*, *15*, 3559–3569.

Key, J. R., Collins, J. B., Fowler, C., & Stone, R. S. (1997). High latitude surface temperature estimates from thermal satellite data. *Remote Sensing of the Environment*, *61*, 302–309.

Kurvonen, L., & Hallikainen, M. (1997). Influence of land-cover category on brightness temperature of snow. *IEEE Transactions on Geoscience and Remote Sensing*, *35*, 367–377.

Langlois, A., & Barber, D. G. (2007a). Advances in seasonal snow water equivalent (SWE) retrieval using in-situ passive microwave measurements over first-year sea ice. *International Journal of Remote Sensing,* In press July 2007, TRES-PAP-2007-0210.

Langlois, A., & Barber, D. G. (2007). Passive microwave remote sensing of seasonal snow covered sea ice. *Progress in Physical Geography*, *31*, 539–573.

Langlois, A., Barber, D. G., & Hwang, B. J. (2007). Development of a snow water equivalent algorithm using passive microwave data over first-year sea ice. *Remote Sensing of Environment*, *106*, 75–88. doi:10.1016/j.rse.2006.07.018

Langlois, A., Mundy, C. J., & Barber, D. G. (2007). Overwintering evolution of geophysical and electrical properties of snow cover over first-year sea ice. *Hydrological Processes*, *21*, 705–716. doi:10.1002/hyp.6407

Livingstone, C. E. (1994). Synthetic aperture radar images of sea ice. In S. Haykin, E. O. Lewis, R. K. Raney, & J. R. Rossiter (Eds.), *Remote sensing of sea ice and icebergs* (pp. 540–569). New York: John Wiley and Sons, Inc.

Mäkynen, M., & Hallikainen, M. (2004). Investigation of C- and X-band backscattering signatures of Baltic Sea ice. *International Journal of Remote Sensing*, *25*, 2061–2086.

Mäkynen, M., & Hallikainen, M. (2005). Passive microwave signature observations of the Baltic Sea ice. *International Journal of Remote Sensing*, *26*, 2081–2106.

Manninen, A. T. (1992). Effects of ice ridge properties on calculated surface backscattering in BEPERS-88. *International Journal of Remote Sensing*, *13*, 2469–2487.

Markus, T., & Cavalieri, D. J. (2000). An enhancement of the NASA Team sea ice algorithm. *IEEE Transactions on Geoscience and Remote Sensing*, *38*, 1387–1398.

Markus, T., Powell, D. C., & Wang, J. R. (2006). Sensitivity of passive microwave snow depth retrievals weather effects and snow evolution. *IEEE Transactions on Geoscience and Remote Sensing*, *44*, 10 pages.

Mätzler, C. (1987). Applications of the interaction of microwaves with natural snow cover. *Remote Sensing Reviews*, *2*, 259–387.

Mätzler, C. (1992). *Passive microwave signature catalogue 1989–1992. Report*, *Vol. 1.* (pp.) University of Berne: Institute of Applied Physics.

Nghiem, S. V., & Bertoia, C. (2001). Multi-polarization C-Band SAR signatures of arctic sea ice. *Proceedings of the IEEE International Geoscience and Remote Sensing Symposium, IGARSS 2001, 9–13, July 2001. Sydney, Australia* (pp. 1792–1794). Piscataway N.J.: IEEE Inc.

Stroeve, J. C., Serreze, M. C., Fetterer, F., Arbetter, T., Meier, W., Maslanik, J., & Knowles, K. (2005). Tracking the Arctic's shrinking ice cover: Another extreme minimum in 2004. *Geophysical Research Letters*, *32* 4 pages.

Sturm, M., Maslanik, J., Perovich, D. K., Stroeve, J. C., Richter-Menge, J., Markus, T., Holmgren, J., Heinrichs, J. F., & Tape, K. (2006). Snow depth and ice thickness measurements from the Beaufort and Chukchi Seas collected during the AMSR-Ice03 Campaign. *IEEE Transactions on Geoscience and Remote Sensing*, *44*, 3009–3020.

Tedesco, M., & Wang, J. R. (2006). Atmospheric correction of AMSR-E brightness temperatures for dry snow cover mapping. *IEEE Geoscience and Remote sensing Letters*, *3*, 320–324.

Wang, J. R., & Tedesco, M. (2007). Identification of atmospheric influences on the estimation of snow water equivalent from AMSR-E measurements. *Remote Sensing of Environment*, *111*, 398–408.

Yackel, J. J., & Barber, D. G. (2007). Observations of snow water equivalent change on landfast first-year sea ice in winter using synthetic aperture radar data. *IEEE Transactions on Geoscience and Remote Sensing*, *45*, 1005–1015.

Yackel, J. J., Barber, D. G., & Papakyriakou, T. N. (2001). On the estimation of spring melt in the North Polynya using RADARSAT-1. *Atmosphere-Ocean*, *39*, 195–208.